

Melting of Charge Density Waves in Low Dimensions

Jeremy M. Shen¹, Alex Stangel², Suk Hyun Sung³, Nishkarsh Agarwal², Ismail El Baggari³, Kai Sun⁴, and Robert Hovden^{2,4,*}

¹Department of Electrical and Computer Engineering, University of Michigan, Ann Arbor, MI. ²Department of Materials Science and Engineering, University of Michigan, Ann Arbor, MI. ³The Rowland Institute at Harvard, Cambridge, MA. ⁴Department of Physics, University of Michigan, Ann Arbor, MI. *e-mail: hovden@umich.edu

Charge density waves (CDWs) are collective electronic states that can reshape and melt, even while confined within a rigid atomic crystal. In two dimensions, melting is predicted to be distinct, proceeding through partially ordered nematic and hexatic states that are neither liquid nor crystal. Here we measure and explain how continuous, hexatic melting of incommensurate CDWs occurs in low-dimensional materials. As a CDW is thermally excited, disorder emerges progressively—initially through smooth elastic deformations that modulate the local wavelength, and subsequently via the nucleation of topological defects. Experimentally, we track three hallmark signatures of CDW melting—azimuthal superlattice peak broadening, wavevector contraction, and integrated intensity decay.

Introduction

Thermal melting of crystals is a dramatic transformation. It is governed by the emergence of topological defects—dislocations that tear the underlying crystalline order. As dislocations proliferate, they disrupt the periodic lattice, driving volumetric expansion and loss of long-range order^{1,2}. Over the past century, it has become clear that melting is dictated by microstructural disorder and dimensionality^{3–5}. In two dimensions, melting can proceed via exotic intermediate phases, such as hexatic and nematic order, that retain orientational coherence despite the loss of translational symmetry—offering partially ordered states that interpolate between a crystalline and liquid phase⁶. Similar hexatic and nematic order of electronic, quantum, and magnetic states are predicted in low-dimensional materials⁷.

Charge density waves (CDWs) represent an electronic analog to classical crystallinity, spontaneously breaking translational symmetry to form periodic modulations in the electronic charge density. These emergent electronic states are often intertwined with other collective phenomena such as superconductivity and Mott insulating behavior and have been observed in materials ranging from transition metal dichalcogenides to cuprates and manganites^{8–10}. Like atomic lattices, CDWs elastically deform and contain topological defects—including dislocations and domain boundaries—that destabilize order¹¹. Electron microscopy has directly imaged such CDW dislocations in pristine crystalline regions of complex oxides. Kourkoutis *et al* have shown that CDWs incommensurate with the crystal lattice exhibit significant local disorder¹². Similar dislocations of the CDW have been reported in the surface states of TaS₂^{13,14} and transient defects of phonon dynamics in 1T-TiSe₂¹⁵. Recently, the creation of CDW dislocations has been observed directly under applied heat¹⁶.

The thermal creation of CDW dislocations is expected to drive the melting of charge density waves, resulting in a loss of long-range CDW order. In two-dimensional 1T-TaS₂, hexatic CDW melting was recently reported¹⁷; however,

the accompanying microstructural evolution—and particularly the observed contraction of the CDW wavevector \mathbf{q} —remains unexplained and seems inconsistent with classical theories of melting. CDW melting occurs at temperatures far below the atomic melting point of the host lattice.

Here we describe melting of incommensurate charge density waves. We show that fluctuations of charge density wave order—through elastic deformation and dislocations—cause characteristic expansion of the CDW with hexatic order. To accommodate CDW expansion within a fixed volume, there is a concomitant reduction in CDW amplitude. This melting of charge density waves has three characteristics visible in diffraction: azimuthal broadening of the wavevector due to hexatic / nematic disorder, contraction of the wavevector due to a reduced packing density of the charge crystal, and a reduction of total diffracted intensity due to attenuation of the charge density wave amplitude. High temperature CDWs in two-dimensional 1T-TaS₂ serve as a model system for CDW melting with clear connection between experiment, computational, and Landau descriptions. A meta-analysis of twenty eight previously reported incommensurate CDW systems—including TaSe₂, BSCMO, LSCO, and TbTe₃—suggests continuous CDW melting processes are broadly present across materials.

Results

Hexatic Melting of 2D Charge Crystals

The CDW is a periodic modulation of valence electron density within the crystal (Fig. 1a) and intimately couples to the atomic lattice through electron-phonon interactions^{18,19}. Electron diffraction is sensitive to atomic movement that directly corresponds to CDW structure. Figure 1b illustrates the CDW structure across temperature. At low temperatures the CDW is ordered (Fig. 1b-bottom) with a well-defined wavevector (\mathbf{q}) (Fig. 1b-ii, iv). As the CDW is thermally excited, disorder emerges progressively—initially

Melting of 2D Charge Density Waves

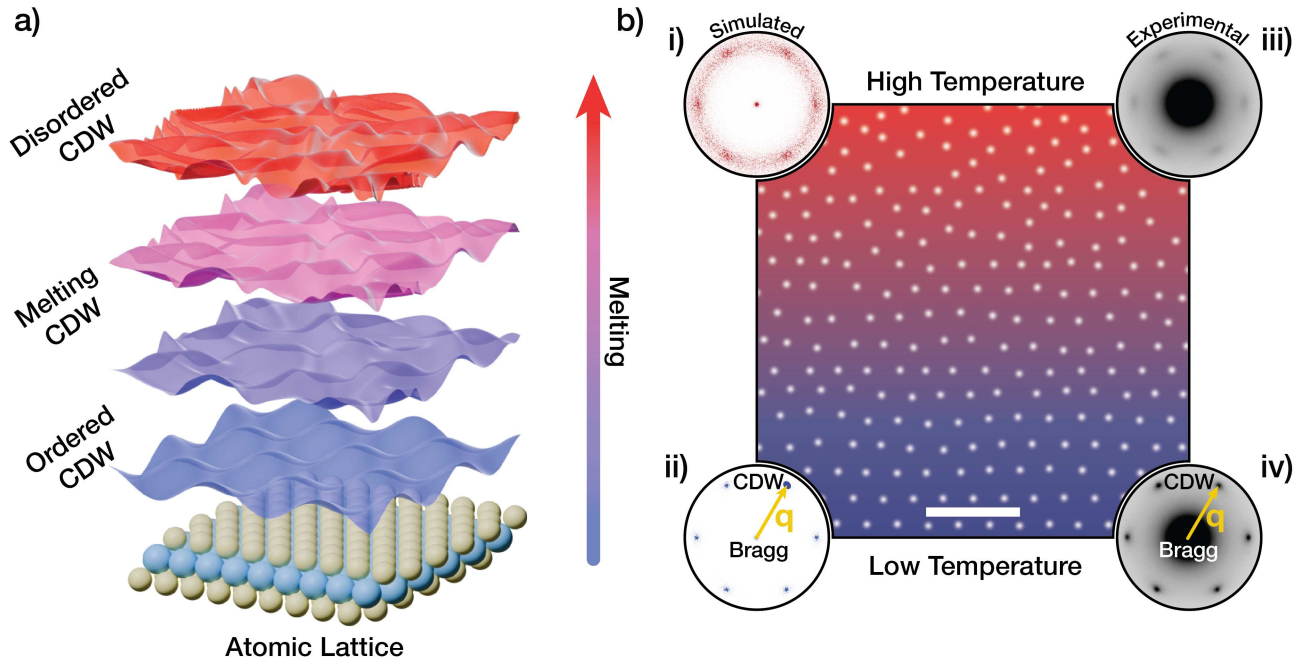


Fig. 1 | Melting of two-dimensional charge density wave. **a)** Illustration of progressively melted 2D CDW. The CDW becomes less spatially coherent, melting independently of the underlying atomic lattice. **b)** Melting of CDW modeled with a lattice of CDW dots. Scale bar is 5 nm. At higher temperatures CDW fluctuations become large, disordered. Comparison of experimental 2D 1T-TaS₂ CDW diffraction (i, iii) with simulated CDW diffraction (ii, iv) at low and high temperatures. Molecular dynamic simulation of CDW melting qualitatively matches experimental electron diffraction.

through smooth elastic deformations that modulate the local wavelength, and subsequently via the nucleation of topological defects that more severely disrupt long-range coherence (Fig. 1b-top).

There are three signatures for hexatic / nematic melting of CDWs that are salient in diffraction: (1) superlattice peaks associated with the CDW blur azimuthally, (2) a shortening of the principal CDW wavevector, (3) a decreasing integrated CDW intensity (Fig. 2). The first two features are known to classical melting of crystal solids²⁰. The third feature is unique to melting of CDWs.

Blurring of CDW Peaks: The primary feature of hexatic melting in diffraction is azimuthal blurring of peaks^{21–25}. Sharp peaks and diffuse rings describe the temperature extremes of ordered and amorphous CDW structures respectively. In-situ electron diffraction of 2D 1T-TaS₂ (Fig. 2b) shows the evolution of an incommensurate CDW superlattice peak as it melts continuously when heated from 408 K to 571 K. Initially, there are six sharp peaks, but upon melting, the peaks begin to blur into the background, becoming more diffuse with increasing temperature. At 571 K the CDW peak in TaS₂ is 3.5 times broader (along the azimuth) than at 408 K (Fig. 2c).

In lower dimensions, translational symmetry is lost before orientational order; a sequence described by the KTHNY theory^{3,6,26,27}. In this continuous progression of the hexatic phase, diffraction peaks broaden azimuthally as translational order decays, while local six-fold coordination—

and thus orientational order—persists (Fig. 1b-i, iii). Six first-order CDW peaks that are radially sharp but azimuthally broad are uniquely attributed to the intermediary hexatic state.

Alongside simulated diffraction patterns of the CDW (Fig. 1b-i,ii) are experimental diffraction patterns (Fig. 1b-iii, iv) taken from 2D 1T-TaS₂ at 408 K and 568 K. In real space, we see how the proliferation of disorder in the charge crystal destroys spatial coherence in the charge density resulting in blurred superlattice peaks. Eventually, the state becomes a fully melted liquid with short-range order. In TaS₂, a complete liquid state was observed using ultrafast electron diffraction by Kogar and colleagues²⁸.

CDW melting is illustrated in Figure 1b using a temperature dependent molecular dynamics simulation of 2D CDWs (See Methods). Melting is computationally modeled by allowing charge density centers to thermally move according to Boltzmann statistics. Charge centers interact through a divergent short-range repulsion—mimicking Pauli exclusion—and a weaker long-range attraction that binds the modulation. The system evolves through an iterative Monte Carlo process until convergence at each temperature.

CDW Wavevector Contraction: During hexatic or nematic melting, the CDW \mathbf{q} -vector contracts due to CDW expansion caused by disorder. Figure 2 experimentally shows the shift towards lower wavevectors in the CDW of 2D 1T-TaS₂. The CDW \mathbf{q} -vector, defined from the Bragg peak to the

superlattice peak, contracts nearly 14% over the temperature regime (408–571 K) (Fig. 2c). The \mathbf{q} -vector contraction happens coincidentally with the peak blurring and decreasing integrated intensity. At high temperatures nearing the liquid phase, the rate of \mathbf{q} -vector contraction accelerates.

The atomic lattice remains relatively unchanged throughout the CDW melting process. Over the CDW melting regime, CDW expansion is roughly 10–500 times larger than thermal expansion in the host atomic crystal^{29–33}. For 1T-TaS₂, the CDW expansion is around 60 times larger than that of the crystal lattice³⁴. Furthermore, CDW transitions occur at temperatures far below the atomic melting point of the host lattice and thus within a nearly constant atomic volume.

The proliferation of CDW dislocations pushes apart the CDW lattice forcing expansion in real-space (\mathbf{q} -vector contraction). When atomic crystals melt, the average lattice spacing increases and the total volume expands. In contrast, CDWs melt within a rigid crystal volume well below the host-lattice melting point. A fully classical treatment of CDW melting in a constant volume unphysically drives up electronic pressure that compresses the CDW (\mathbf{q} -vector expansion) (Supplementary Fig. 1). Thus, classical melting in a fixed volume contradicts the observed CDW melting behavior where the CDW lattice expands (\mathbf{q} -vector contracts). For CDWs the total amplitude of charge density centers need not be conserved. A description of CDW melting requires a spatially fluctuating charge density amplitude—akin to a grand canonical ensemble.

CDW Intensity Weakens: CDW melting departs from classical solid melting, proceeding with the simultaneous emergence of disorder and localized CDW amplitude collapse. A local CDW collapse around defect centers relieves electronic pressure without causing volumetric expansion of the CDW. This effectively lowers the number of charge density peaks as temperature rises and the average real space wavelength increases (\mathbf{q} contracts) while the system minimizes its free energy within a constant volume (Supplementary Fig. 1).

The decreasing integrated intensity of CDW superlattice peaks is a direct measurement of CDW attenuation during melting. In TaS₂, the integrated peak intensity halves over the temperature regime (408–571 K) (Fig. 2c). Simulations closely match experimental diffraction of the continuous contraction of the incommensurate CDW wavevector and the decay of the peak's integrated intensity (Fig. 3a–f). Note, the integrated intensity is distinct from the CDW peak height which will decrease as it broadens.

Nearly Universal CDW Melting Behavior

Characteristic continuous melting of incommensurate CDWs is observed in nearly all (quasi-) 2D CDW systems at elevated temperatures. We compile a meta-study of melting behavior of CDWs probed via X-ray, neutron, and electron diffraction (Fig. 3g–l, Supplementary Figs. 2–4). Incommensurate CDWs in bulk TMDs such as 2H-TaSe₂ and

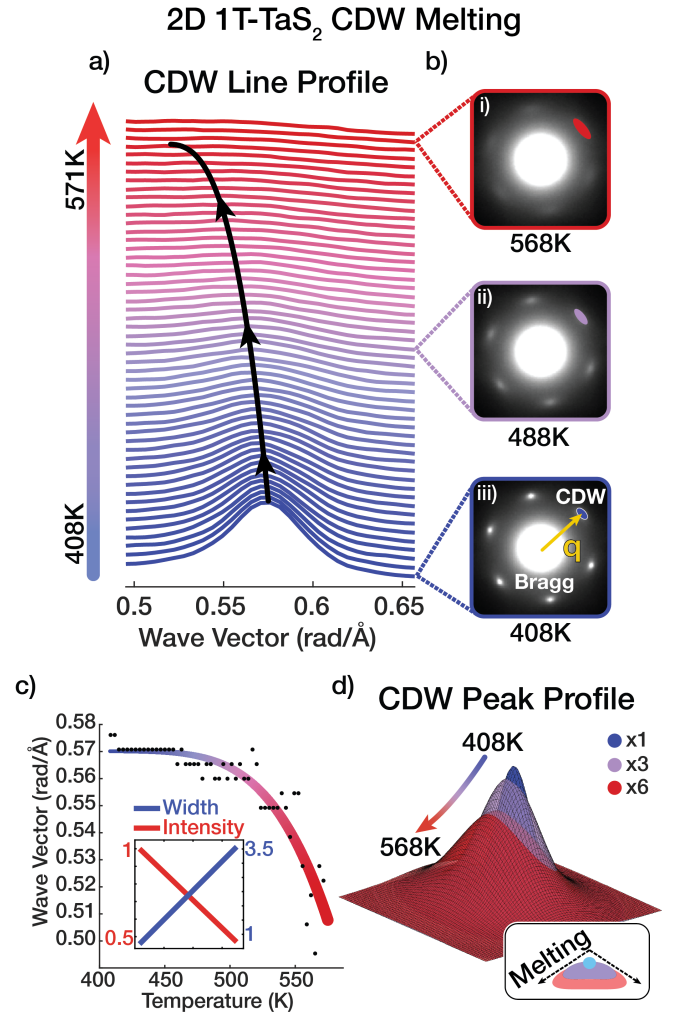


Fig. 2 | Evolution of CDW melting in diffraction (2D 1T-TaS₂). **a)** Experimental line profile through CDW superlattice peaks in **(b)**. The CDW peaks are initially sharp (i) but azimuthally blur and decrease in intensity continuously (ii,iii). From 408 K to 571 K, the \mathbf{q} -vector contracts by 14%. Black line is a guide to the eye. **c)** Superlattice peak \mathbf{q} -vector, width, and integrated intensity quantified. These features of CDW melting evolve concurrently. **d)** Superlattice peak profiles at 408 K (blue), 488 K (purple), and 568 K (red) scaled by $1\times$, $3\times$, and $6\times$, respectively. Inset) Cartoon depiction of superlattice peak evolution: peak position shift to lower wavenumbers and peak blurring.

2H-NbSe₂ melt similarly to 2D 1T-TaS₂^{35,38–40}. We find this behavior occurs in 2-, 3-, and 4-fold in-plane crystal symmetries. Wavevector contraction, peak width increase, and integrated intensity decrease are observed in melting of incommensurate CDWs in manganites (BSCMO)^{12,16,41–43}, 2D metals such as (K_{1-x}Rb_x)₃Cu₈S₆ and LaAgSb₂^{37,44,45}, rare earth tellurides TbTe₃ and Gd₂Te₅^{31,46}, and other CDW systems such as BaNi₂As₂, UPt₂Si₂, LaPt₂Si₂, and CuV₂S₄^{33,47–49}. Croft et al. report these melting features in one cuprate system La_{1.88}Sr_{0.12}CuO₄³⁶. A scanning tunneling microscopy study of the 2D surface CDW in NbSe₃ shows consistent melting behavior⁵⁰.

However, it should be noted that the wavevector evolution of incommensurate CDWs in cuprates varies greatly with doping concentration and both contraction and expansion of the CDW has been reported^{36,51–53}. Melting of

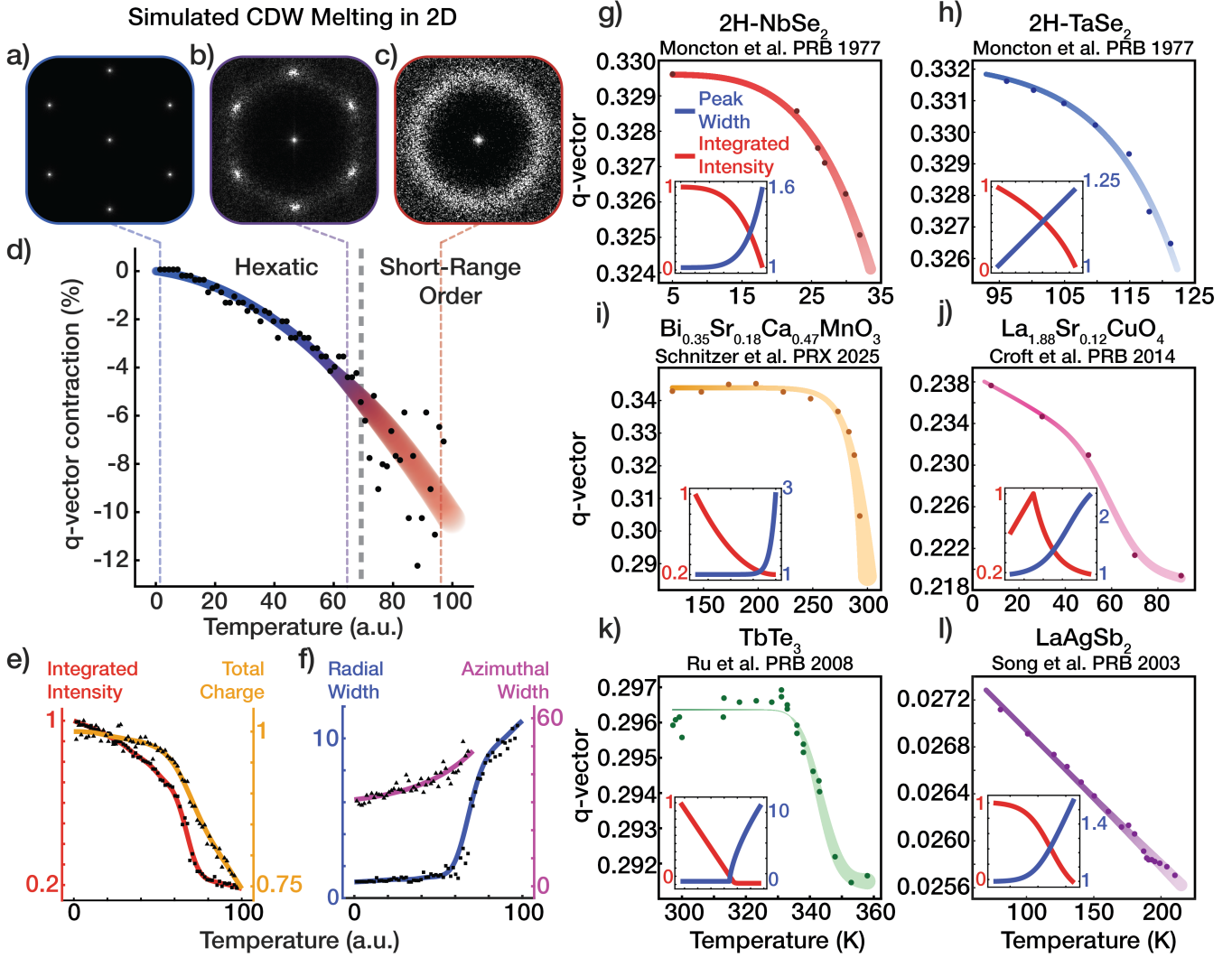


Fig. 3 | Melting of incommensurate CDWs in previously reported literature and a simulated CDW. **a–c)** Simulated diffraction patterns of melted charge lattice with **(d)** wavevector contraction, **(e)** integrated intensity decay, and **(f)** peak width broadening. **e)** The number of CDW peaks decreases with melting. **f)** (purple) The superlattice peaks blur azimuthally in the hexatic regime before becoming amorphous rings. **f)** (blue) There is slight radial broadening in the hexatic regime which rapidly accelerates as it becomes amorphous. Wavevector contraction, peak broadening, and integrated intensity decrease quantified for **(g, h)** 2D transition metal dichalcogenides³⁵, **(i)** manganites¹⁶, **(j)** cuprates³⁶, **(k)** rare-earth tellurides³¹, and **(l)** 2D metals³⁷. Fitted lines are guides to the eye, where line width and color intensity is proportional to CDW peak width and integrated intensity respectively. Many more material systems (see Supplementary Figs. 2–4) undergo a continuous melting process for incommensurate CDWs.

(quasi-) 1D CDWs show no clear preference for wavevector contraction or expansion (Supplementary Figs. 4, 5). SmNiC_2 , Ta_2NiSe_7 , U_2Ti , and $\text{Er}_5\text{Ir}_4\text{Si}_{10}$ exhibit wavevector contraction^{54–57}, while $\text{Ho}_5\text{Ir}_4\text{Si}_{10}$, blue bronzes, and NbSe_3 exhibit wavevector expansion^{58–61}. Wavevector expansion is observed in orthorhombic TaS_3 , while in the monoclinic polymorph, the wavevector remains unchanged⁶².

Fluctuation Driven CDW Expansion

The physical origin of CDW expansion can be understood by combining insights from two seminal works^{63,64}. We show that disorder and fluctuations arising from CDW melting naturally lead to an expansion of the CDW wavelength.

To illustrate CDW wavelength expansion, we consider a unidirectional CDW with wavevector \mathbf{q} and order parameter $\psi(\mathbf{r}) = Ae^{i\mathbf{q}\cdot\mathbf{r}}$ (Fig. 4a,c). The theory readily gen-

eralizes to more complex cases, such as hexagonal CDWs formed by a superposition of three unidirectional components (Fig. 4e). We define $\mathbf{r} = (x, z)$, with x and z denoting directions perpendicular and parallel to \mathbf{q} , respectively. Melting of the CDW introduces strong fluctuations and disorder, resulting in dislocations and distortions of the CDW wavefront (Fig. 4b,d). These effects are captured by fluctuating the order parameter

$$\psi(\mathbf{r}) = A(\mathbf{r})e^{iq(z+u(\mathbf{r}))}, \quad (1)$$

where $A(\mathbf{r})$ and $qu(\mathbf{r})$ describe amplitude and phase fluctuations, respectively. Here we focus on fluctuating displacements of the wavefront, $u(\mathbf{r})$, that are prevalent in 2D CDW melting.

As pointed out by McMillan⁶³, for an incommensurate CDW, the frequency of phase fluctuations vanishes in the long-wavelength limit ($k \rightarrow 0$), implying that, to leading-

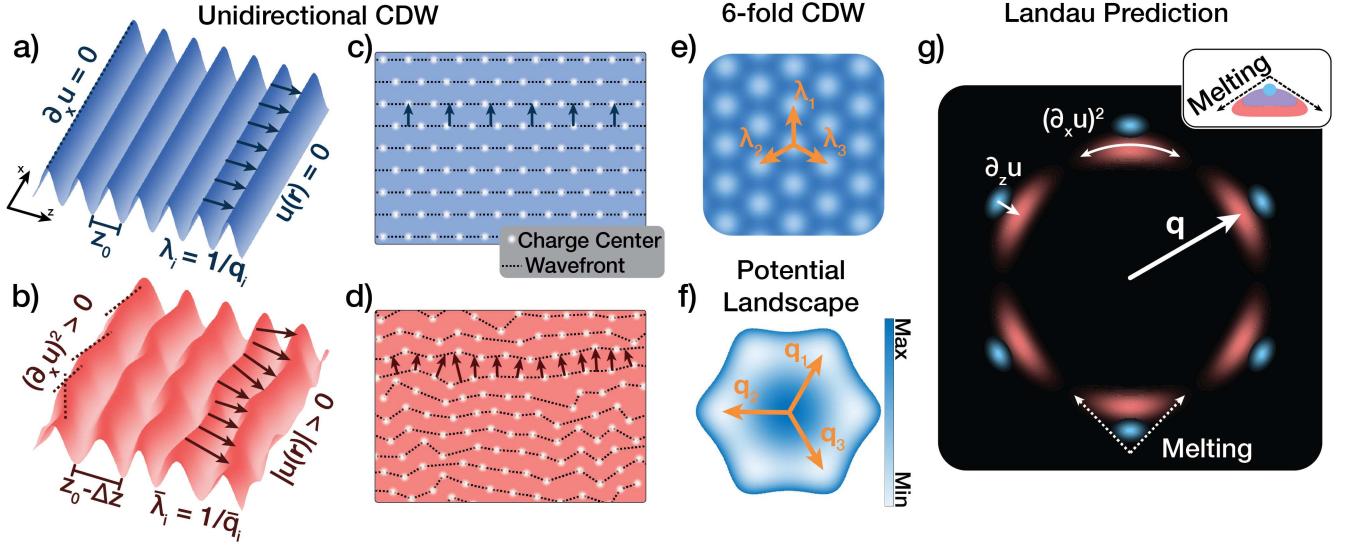


Fig. 4 | Fluctuation driven melting of charge density waves. Illustration of ordered (a) and disordered (b) unidirectional CDWs. Fluctuations in the wavefront $u(\mathbf{r})$ drive a wavelength increase by $-\Delta Z$. In the charge lattice, planes of charge centers are discrete representations of the CDW wavefront (c, d). Incommensurate CDW in 2D 1T-TaS₂ is a triple-CDW system with 6-fold symmetry (e). Here, we use λ_i to denote real space CDW wavelength. (f) Potential landscape in reciprocal space constructed with Landau theory. (g) Predicted peak evolution of wavefronts consistent with the Landau free energy landscape. Melting drives CDW wavevector contraction and peak broadening.

order, the free energy includes only terms such as $(\partial_x u)^2$ and $(\partial_z u)^2$. While sufficient for many purposes, these terms alone cannot explain melt-induced CDW expansion where higher-order terms become essential. Fortunately, Grinstein and Pelcovits⁶⁴ derived such nonlinear contributions in their study of smectics and 1D solids. Combining their results with McMillan’s theory, we obtain the effective free energy of a disordered CDW:

$$H = \frac{1}{2} K A^2 q_0^4 \int d^2 r \left\{ C_0 (\partial_x u)^2 + \frac{1}{2 q_0^2} (\partial_x^2 u)^2 + 2 (\partial_z u)^2 + 2 \partial_z u (\partial_x u)^2 + \frac{1}{2} [(\partial_x u)^2]^2 + \text{higher order terms} \right\} \quad (2)$$

The first three terms are quadratic in u and describe linear responses; the remaining terms govern nonlinear behavior. In smectics (Grinstein and Pelcovits), continuous rotational symmetry prohibits the $(\partial_x u)^2$ term, enforcing $C_0 = 0$. However, for CDWs in crystals with discrete rotational symmetry (Fig. 4f), C_0 is symmetry-allowed and must be included to match McMillan’s theory (see Supplementary Materials). In addition, the presence of the lattice can also renormalize other coefficients, but we neglect such corrections at leading order.

The free energy contains two key deformation modes: $\partial_x u$, describing CDW wavefront distortions, and $\partial_z u$ controlling the wavevector magnitude—i.e., contraction ($\partial_z u > 0$) or expansion ($\partial_z u < 0$) of the CDW (corresponding to an expansion and contraction of \mathbf{q} , respectively). At quadratic order, these modes are decoupled. However, the cubic term $\partial_z u (\partial_x u)^2$, the leading-order nonlinear term allowed by symmetry, couples them and plays a pivotal role. In smectics, this cubic coupling underlies fluctuation-driven

renormalizations⁶⁴ and stretch-induced buckling instabilities⁶⁵.

In the context of CDW melting, the nonlinear term plays a similarly crucial role. Melting introduces disorder and dislocations, leading to an increased $\langle (\partial_x u)^2 \rangle$, which quantifies wavefront distortions. Due to the positive coefficient of this cubic coupling, a negative $\partial_z u$ lowers the free energy, indicating that wavevector contraction—and thus wavelength expansion—is energetically favored. As a result, crumpled CDW wavefronts due to the melting naturally induce an expansion of the CDW wavelength, as illustrated in Figure 4g. The peak evolution in Figure 4g is empirically constructed for consistency with the Landau model and experimental observations in TaS₂.

Amplitude fluctuations of the CDW become important around CDW dislocations. Outside of these regions the CDW is more uniform and the amplitude changes are small¹². This behavior can be captured through a typical Landau expansion of $\psi(\mathbf{r})$ where amplitude fluctuations are allowed. In this picture, the amplitude of the CDW couples directly to disorder in its phase as $A^2(\mathbf{r})(\nabla q u(\mathbf{r}))^2$. As the CDW structure becomes disordered, the amplitude of the CDW will decrease. In regions around dislocation cores, the phase term $(\nabla q u(\mathbf{r}))^2$ diverges causing total amplitude collapse.

Conclusion

In summary, we show that 2D incommensurate charge density waves melt continuously through intermediate hexatic and nematic phases. \mathbf{q} -vector contraction and CDW amplitude reduction are an intrinsic feature of CDW dislocations introduced during the melting process. CDW melting is distinct from classical melting: the emergence of CDW dis-

locations drives the disappearance of local charge-density that relieves electronic pressure, minimizes its free energy, and accommodates contraction of \mathbf{q} within a fixed volume. Melting gives the appearance of an increase in incommensurability. However, long-range CDW order is not present at elevated temperatures and the incommensurate \mathbf{q} -vector is tied to CDW fluctuations. This melting behavior is found in nearly all incommensurate 2D CDW systems with various crystal symmetry. This work highlights how subtle changes in the diffraction of CDWs manifest from complex microstructure in the real space order parameter of quantum states.

Methods

Electron Microscopy

In-situ SAED was performed on Thermo Fisher Scientific (TFS) Talos (operated at 200 keV, 850 nm SA aperture) with Protochips Fusion Select holder and Gatan OneView Camera.

2D 1T-TaS₂ was made using an endotaxial synthesis process previously described¹⁷. Here, monolayers of 1T-TaS₂ (octohedral coordination) are embedded and isolated within bulk metallic TaS₂ (prismatic coordination). TEM specimens were prepared by exfoliating bulk 1T-TaS₂ crystals onto polydimethylsiloxane (PDMS) gel stamp. The sample was then transferred to TEM grids using a home-built transfer stage. 2D 1T-TaS₂ polytype was synthesized by heating 1T-TaS₂ to 720 K in high vacuum ($\sim 10^{-7}$ Torr) for ~ 10 min, then brought down to room temperature¹⁷.

CDW superlattice peaks are anisotropically distributed around each Bragg peak. We average the six first order Bragg peaks and surrounding superlattice peaks to obtain the CDW diffraction pattern (Supplementary Fig. 7)¹⁷.

Simulating Charge Density Wave Melting

Hexatic CDW melting is simulated by mobile charge centers which hop according to Boltzmann statistics ($e^{-\frac{\Delta E}{kT}}$) through a Monte Carlo process. The interaction energy between charge centers is calculated using a shifted Lennard Jones potential truncated at 100 Å. This effectively treats high-temperature CDWs as a phenomenological charge crystal. CDW amplitude collapse is modeled with the removal of charge centers at topological defect sites. The simulation is of a grand canonical ensemble (varying particle count, constant volume and temperature). Every 150 iterations, we remove a charge center with the lowest Ψ_6 order parameter until we reach a minimum energy configuration. The melted CDW in Fig. 3a–f starts with a particle count of 2016 charge centers in a fixed 2D volume with periodic boundary conditions. We ensure energy convergence at steady state. Temperature and energy were scaled to be consistent with observed 2D 1T-TaS₂ incommensurate CDW melting.

Diffraction of simulated CDWs in a 2D 1T-TaS₂ crystal is calculated using the concomitant periodic lattice displacement (PLD) of the atomic potentials. The displacement amplitude is proportional to the charge density gradient with a max displacement of 7 pm. Electron diffraction is kinematically simulated under flat Ewald Sphere approximations using the Fourier transform of the displaced atomic lattice.

Meta-analysis Data Collection

Meta-analysis data was digitally extracted from wavevector, peak width, and integrated intensity vs. temperature plots or peak profiles from digital copies of each manuscript. In some instances the integrated intensity or peak width was not reported. References to each manuscript is included.

Data Availability

In-situ SAED of 2D TaS₂ CDW is available at <https://doi.org/10.5281/zenodo.15335279>.

Code Availability

The code used to simulate and visualize 2D CDW melting (Fig. 3a–f) is available at <https://doi.org/10.5281/zenodo.15334715>.

References

1. Kuhlmann-Wilsdorf, D. Theory of Melting. *Phys. Rev.* **140**, A1599–A1610 (1965).
2. Mo, M. Z. *et al.* Heterogeneous to homogeneous melting transition visualized with ultrafast electron diffraction. *Science* **360**, 1451–1455 (2018).
3. Kosterlitz, J. M. & Thouless, D. J. Ordering, metastability and phase transitions in two-dimensional systems. *J. Phys. C: Solid State Phys.* **6**, 1181 (1973).
4. Mermin, N. D. & Wagner, H. Absence of ferromagnetism or antiferromagnetism in one- or two-dimensional isotropic Heisenberg models. *Phys. Rev. Lett.* **17**, 1133 (1966).
5. Peierls, R. Bemerkungen über Umwandlungstemperaturen. *Helv. Phys. Acta* **7** (1934).
6. Halperin, B. I. & Nelson, D. R. Theory of Two-Dimensional Melting. *Phys. Rev. Lett.* **41**, 121–124 (1978).
7. Nie, L., Tarjus, G. & Kivelson, S. A. Quenched disorder and vestigial nematicity in the pseudogap regime of the cuprates. *Proc. Natl. Acad. Sci.* **111**, 7980–7985 (2014).
8. Cho, K. *et al.* Using controlled disorder to probe the interplay between charge order and superconductivity in NbSe₂. *Nat. Commun.* **9**, 2796 (2018).
9. Ichimura, M., Fujita, M. & Nakao, K. Charge-density wave with imperfect nesting and superconductivity. *Phys. Rev. B* **41**, 6387–6393 (1990).
10. Chang, J. *et al.* Direct observation of competition between superconductivity and charge density wave order in YBa₂Cu₃O_{6.67}. *Nat. Phys.* **8**, 871–876 (2012).
11. Savitzky, B. H. *et al.* Bending and breaking of stripes in a charge ordered manganite. *Nat. Commun.* **8**, 1883 (2017).
12. El Baggari, I. *et al.* Nature and evolution of incommensurate charge order in manganites visualized with cryogenic scanning transmission electron microscopy. *Proc. Natl. Acad. Sci.* **115**, 1445–1450 (2018).
13. Dai, H., Chen, H. & Lieber, C. M. Weak pinning and hexatic order in a doped two-dimensional charge-density-wave system. *Phys. Rev. Lett.* **66**, 3183–3186 (1991).
14. Vogelgesang, S. *et al.* Phase ordering of charge density waves traced by ultrafast low-energy electron diffraction. *Nat. Phys.* **14**, 184–190 (2018).

15. Cheng, Y. *et al.* Ultrafast formation of topological defects in a two-dimensional charge density wave. *Nat. Phys.* **20**, 54–60 (2024).
16. Schnitzer, N. *et al.* Atomic-Scale Tracking of Topological Defect Motion and Incommensurate Charge Order Melting. *Phys. Rev. X* **15**, 011007 (2025).
17. Sung, S. H. *et al.* Endotaxial stabilization of 2D charge density waves with long-range order. *Nat. Commun.* **15**, 1403 (2024).
18. Peierls, R. Zur Theorie der elektrischen und thermischen Leitfähigkeit von Metallen. *Ann. Phys.* **396**, 121–148 (1930).
19. Overhauser, A. W. Observability of charge-density waves by neutron diffraction. *Phys. Rev. B* **3**, 3173 (1971).
20. Sulyanova, E. A. *et al.* Structural Evolution of Colloidal Crystal Films in the Process of Melting Revealed by Bragg Peak Analysis. *Langmuir* **31**, 5274–5283 (2015).
21. Williams, P. M., Parry, G. S. & Scrub, C. B. Diffraction evidence for the Kohn anomaly in 1T-TaS₂. *Philos. Mag.* **29**, 695–699 (1974).
22. Van Landuyt, J., Van Tendeloo, G. & Amelinckx, S. Electron diffraction study of inter- and intrapolytypic phase transitions in transition metal dichalcogenides. I. Electron diffraction patterns. *Phys. Status Solidi A* **26**, 359–376 (1974).
23. Ishiguro, T. & Sato, H. Electron microscopy of phase transformations in 1T-TaS₂. *Phys. Rev. B* **44**, 2046 (1991).
24. Welberry, T. R. & Withers, R. L. Optical transforms of disordered systems displaying diffuse intensity loci. *J. Appl. Crystallogr.* **20**, 280–288 (1987).
25. Dai, H. & Lieber, C. M. Charge density wave pinning and disorder in two dimensions. *J. Phys. Chem.* **97**, 2362–2367 (1993).
26. Kosterlitz, J. M. & Thouless, D. J. Long range order and metastability in two dimensional solids and superfluids. (Application of dislocation theory). *Journal of Physics C: Solid State Physics* **5**, L124 (1972).
27. Young, A. P. Melting and the vector Coulomb gas in two dimensions. *Phys. Rev. B* **19**, 1855–1866 (1979).
28. Lee, J. S., Sutter, T. M., Karapetrov, G., Musumeci, P. & Kogar, A. Topological phase transition to a hidden charge density wave liquid. *unpublished* (2025).
29. Sezerman, O., Simpson, A. & Jericho, M. Thermal expansion of 1T-TaS₂ and 2H-NbSe₂. *Solid State Communications* **36**, 737–740. ISSN: 0038-1098 (1980).
30. Nakayama, S. *et al.* Anisotropy in thermal expansion of La_{2-x}Sr_xCuO₄. *Physica C: Superconductivity* **235-240**, 1283–1284. ISSN: 0921-4534 (1994).
31. Ru, N. *et al.* Effect of chemical pressure on the charge density wave transition in rare-earth tritellurides RTe₃. *Phys. Rev. B* **77**, 035114 (2008).
32. Bud'ko, S. L. *et al.* Thermal expansion and magnetostriction of pure and doped RAgSb₂ (R = Y, Sm, La) single crystals. *Journal of Physics: Condensed Matter* **20**, 115210 (2008).
33. Falkowski, M., Doležal, P., Andreev, A. V., Duverger-Nédellec, E. & Havela, L. Structural, thermodynamic, thermal, and electron transport properties of single-crystalline LaPt₂Si₂. *Phys. Rev. B* **100**, 064103 (2019).
34. Robbins, M. O. & and, E. A. M. X-ray studies of the charge-density wave transitions in TaS₂. *Philosophical Magazine* **42**, 705–715 (1980).
35. Moncton, D. E., Axe, J. D. & DiSalvo, F. J. Neutron scattering study of the charge-density wave transitions in 2H-TaSe₂ and 2H-NbSe₂. *Phys. Rev. B* **16**, 801–819 (1977).
36. Croft, T. P., Lester, C., Senn, M. S., Bombardi, A. & Hayden, S. M. Charge density wave fluctuations in La_{2-x}Sr_xCuO₄ and their competition with superconductivity. *Phys. Rev. B* **89**, 224513 (2014).
37. Song, C. *et al.* Charge-density-wave orderings in LaAgSb₂: An X-ray scattering study. *Phys. Rev. B* **68**, 035113 (2003).
38. Fleming, R. M., Moncton, D. E., McWhan, D. B. & DiSalvo, F. J. Broken Hexagonal Symmetry in the Incommensurate Charge-Density Wave Structure of 2H-TaSe₂. *Phys. Rev. Lett.* **45**, 576–579 (1980).
39. Koyama, Y. & Onozuka, T. Electron Microscopy Study of the Charge-Density-Wave Transition in 2H-TaSe₂. *Mater. Trans. JIM* **31**, 636–640 (1990).
40. Feng, Y. *et al.* Itinerant density wave instabilities at classical and quantum critical points. *Nat. Phys.* **11**, 865–871 (2015).
41. Chen, C. H. & Cheong, S.-W. Commensurate to Incommensurate Charge Ordering and Its Real-Space Images in La_{0.5}Ca_{0.5}MnO₃. *Phys. Rev. Lett.* **76**, 4042–4045 (1996).
42. Chen, C. H., Mori, S. & Cheong, S.-W. Anomalous Melting Transition of the Charge-Ordered State in Manganites. *Phys. Rev. Lett.* **83**, 4792–4795 (1999).
43. Milward, G. C., Calderón, M. J. & Littlewood, P. B. Electronically soft phases in manganites. *Nature* **433**, 607–610 (2005).
44. Fleming, R. M., ter Haar, L. W. & DiSalvo, F. J. X-ray scattering study of charge-density waves in K₃Cu₈S₆. *Phys. Rev. B* **35**, 5388–5391 (1987).
45. Sato, H., Kojima, N. & Kagoshima, S. Structural Phase Transitions of the Quasi Two-Dimensional Metal (K_{1-x}Rb_x)Cu₈S₆: X-Ray Scattering Studies. *J. Phys. Soc. Japan* **62**, 2051–2061 (1993).
46. Shin, K. Y. *et al.* Observation of two separate charge density wave transitions in Gd₂Te₅ via transmission electron microscopy and high-resolution X-ray diffraction. *J. Alloys Compd.* **489**, 332–335 (2010).
47. Souliou, S. M. *et al.* Soft-Phonon and Charge-Density-Wave Formation in Nematic BaNi₂As₂. *Phys. Rev. Lett.* **129**, 247602 (2022).
48. Lee, J. *et al.* Charge density wave with anomalous temperature dependence in UPt₂Si₂. *Phys. Rev. B* **102**, 041112 (2020).
49. Fleming, R. M., DiSalvo, F. J., Cava, R. J. & Waszczak, J. V. Observation of charge-density waves in the cubic spinel structure CuV₂S₄. *Phys. Rev. B* **24**, 2850–2853 (1981).
50. Brun, C., Wang, Z.-Z., Monceau, P. & Brazovskii, S. Surface Charge Density Wave Phase Transition in NbSe₃. *Phys. Rev. Lett.* **104**, 256403 (2010).
51. Miao, H. *et al.* Formation of Incommensurate Charge Density Waves in Cuprates. *Phys. Rev. X* **9**, 031042 (2019).
52. Lee, S. *et al.* Generic character of charge and spin density waves in superconducting cuprates. *Proc. Natl. Acad. Sci.* **119**, e2119429119 (2022).
53. Tabis, W. *et al.* Synchrotron x-ray scattering study of charge-density-wave order in HgBa₂CuO_{4+δ}. *Phys. Rev. B* **96**, 134510 (2017).
54. Shimomura, S. *et al.* Charge-Density-Wave Destruction and Ferromagnetic Order in SmNiC₂. *Phys. Rev. Lett.* **102**, 076404 (2009).
55. Fleming, R. M., Sunshine, S. A., Chen, C. H., Schneemeyer, L. F. & Waszczak, J. V. Defect-inhibited incommensurate distortion in Ta₂NiSe₇. *Phys. Rev. B* **42**, 4954–4959 (1990).
56. Stevens, C. R., Hermann, A., Huxley, A. & Wermeille, D. Incommensurate charge density wave order in U₂Ti. *Phys. Rev. B* **109**, 125116 (2024).
57. Galli, F. *et al.* Charge-Density-Wave Transitions in the Local-Moment Magnet Er₅Ir₄Si₁₀. *Phys. Rev. Lett.* **85**, 158–161 (2000).
58. Tseng, C. M., Chen, C. H. & Yang, H. D. Direct observation of charge-density waves in Ho₅Ir₄Si₁₀. *Phys. Rev. B* **77**, 155131 (2008).
59. Moudden, A. H., Elmiger, M., Shapiro, S. M., Collins, B. T. & Greenblatt, M. Neutron-scattering investigation of the charge-density wave in Ti_{0.3}MoO₃. *Phys. Rev. B* **44**, 3324–3327 (1991).
60. Fleming, R. M., Schneemeyer, L. F. & Moncton, D. E. Commensurate-incommensurate transition in the charge-density-wave state of K_{0.30}MoO₃. *Phys. Rev. B* **31**, 899–903 (1985).
61. Moudden, A. H., Axe, J. D., Monceau, P. & Levy, F. q₁ charge-density wave in NbSe₃. *Phys. Rev. Lett.* **65**, 223–226 (1990).
62. Roucau, C. New results obtained by electron diffraction on the one-dimensional conductors TaS₃ and NbS₃. *J. Phys. Colloq.* **44**, C3–1725 (1983).
63. McMillan, W. L. Landau theory of charge-density waves in transition-metal dichalcogenides. *Phys. Rev. B* **12**, 1187–1196 (1975).
64. Grinstein, G. & Pelcovits, R. A. Anharmonic Effects in Bulk Smectic Liquid Crystals and Other “One-Dimensional Solids”. *Phys. Rev. Lett.* **47**, 856–859 (1981).
65. Chaikin, P. M. & Lubensky, T. C. *Principles of Condensed Matter Physics* (Cambridge University Press, Cambridge, 1995).

Acknowledgements

R.H., A.S., J.M.S. acknowledge support from the U.S. Department of Energy, Basic Energy Sciences, under award

DE-SC0024147. N.A. and K.S. were supported by the National Science Foundation through the Materials Research Science and Engineering Center at the University of Michigan, Award No. DMR-2309029. Experiments were conducted using the Michigan Center for Materials Characterization (MC2). This research was supported in part through computational resources and services provided by Advanced Research Computing at the University of Michigan, Ann Arbor.

Author Contributions

S.H.S, J.M.S, R.H. analyzed electron diffraction data. J.M.S., A.S., S.H.S., I.E.B., R.H., and K.S. provided theoretical interpretation. J.M.S., S.H.S., N.A., R.H. ran computational models of CDW melting. A.S. and K.S. developed analytic Landau description of CDW melting. J.M.S., A.S., K.S., and R.H. prepared the manuscript. All authors reviewed and edited the manuscript.

Ethics Declarations

Competing Interests

The authors declare no competing interests.

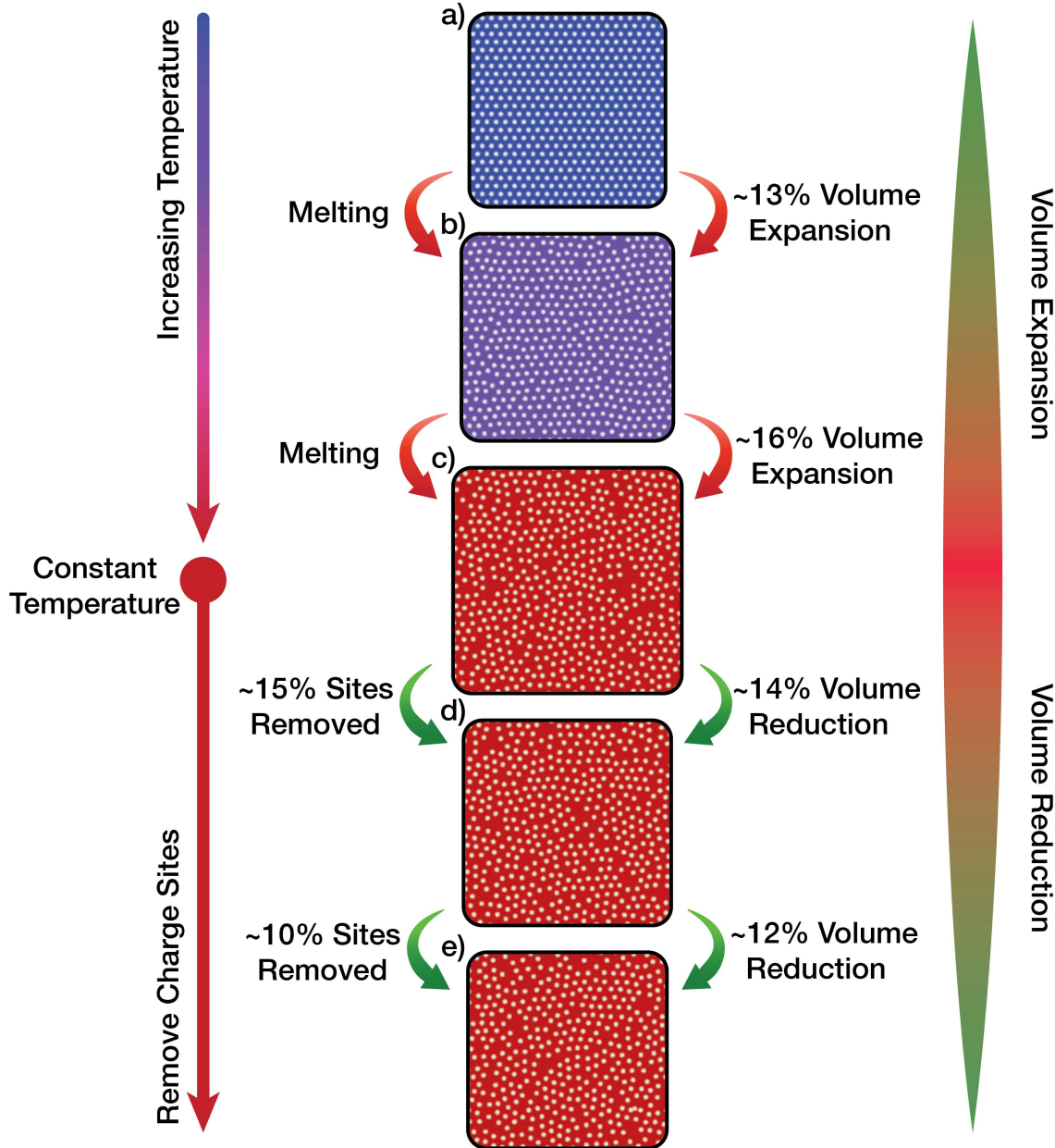
Supplementary Information for

Melting of Charge Density Waves in Low Dimensions

Jeremy M. Shen¹, Alex Stangel², Suk Hyun Sung³, Nishkarsh Agarwal², Ismail El Baggari³, Kai Sun⁴, and Robert Hovden^{2,4,*}

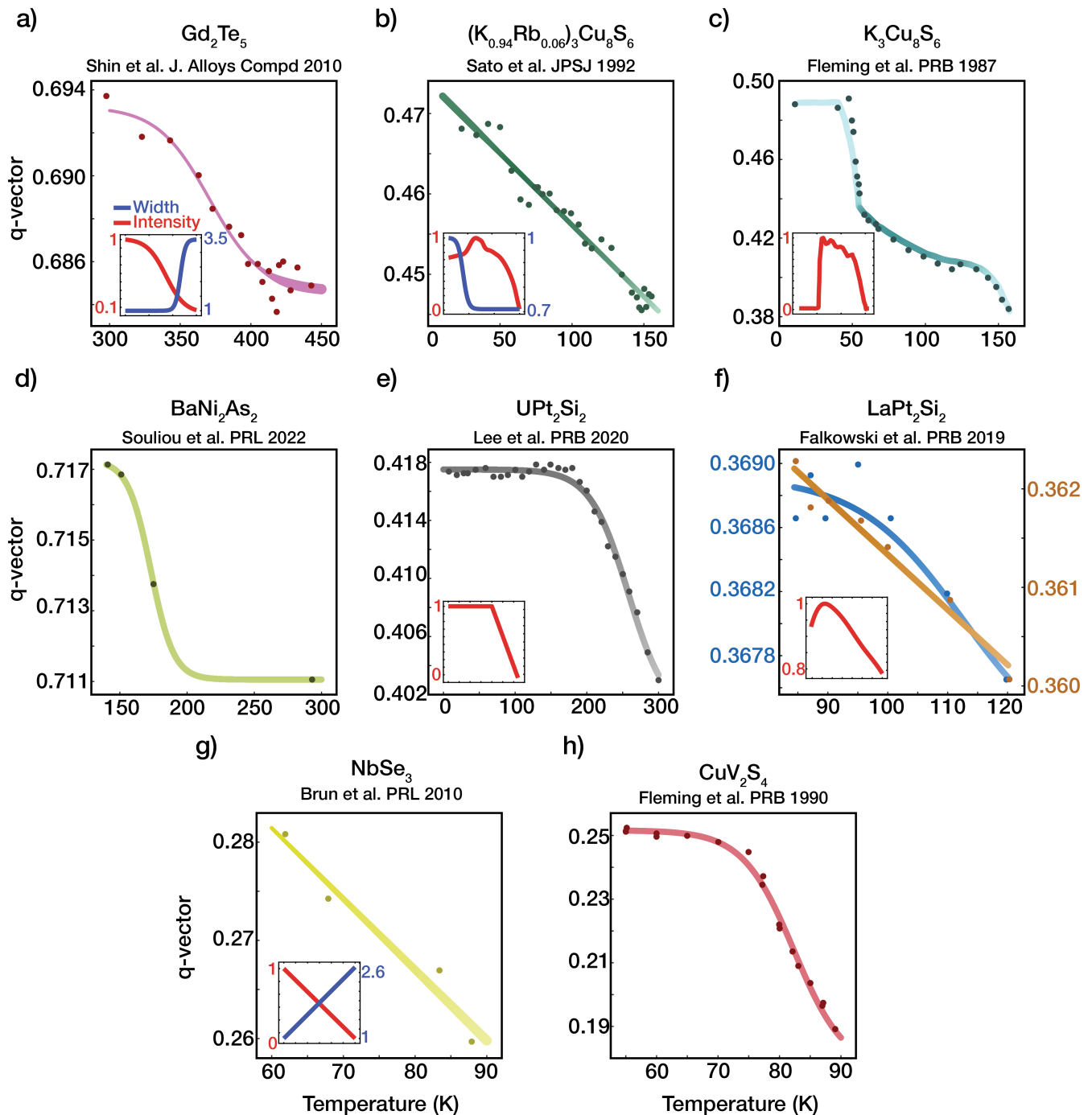
¹Department of Electrical and Computer Engineering, University of Michigan, Ann Arbor, MI. ²Department of Materials Science and Engineering, University of Michigan, Ann Arbor, MI. ³The Rowland Institute at Harvard, Cambridge, MA. ⁴Department of Physics, University of Michigan, Ann Arbor, MI. *e-mail: hovden@umich.edu

1 Melting with Volume Reduction and Charge Relaxation



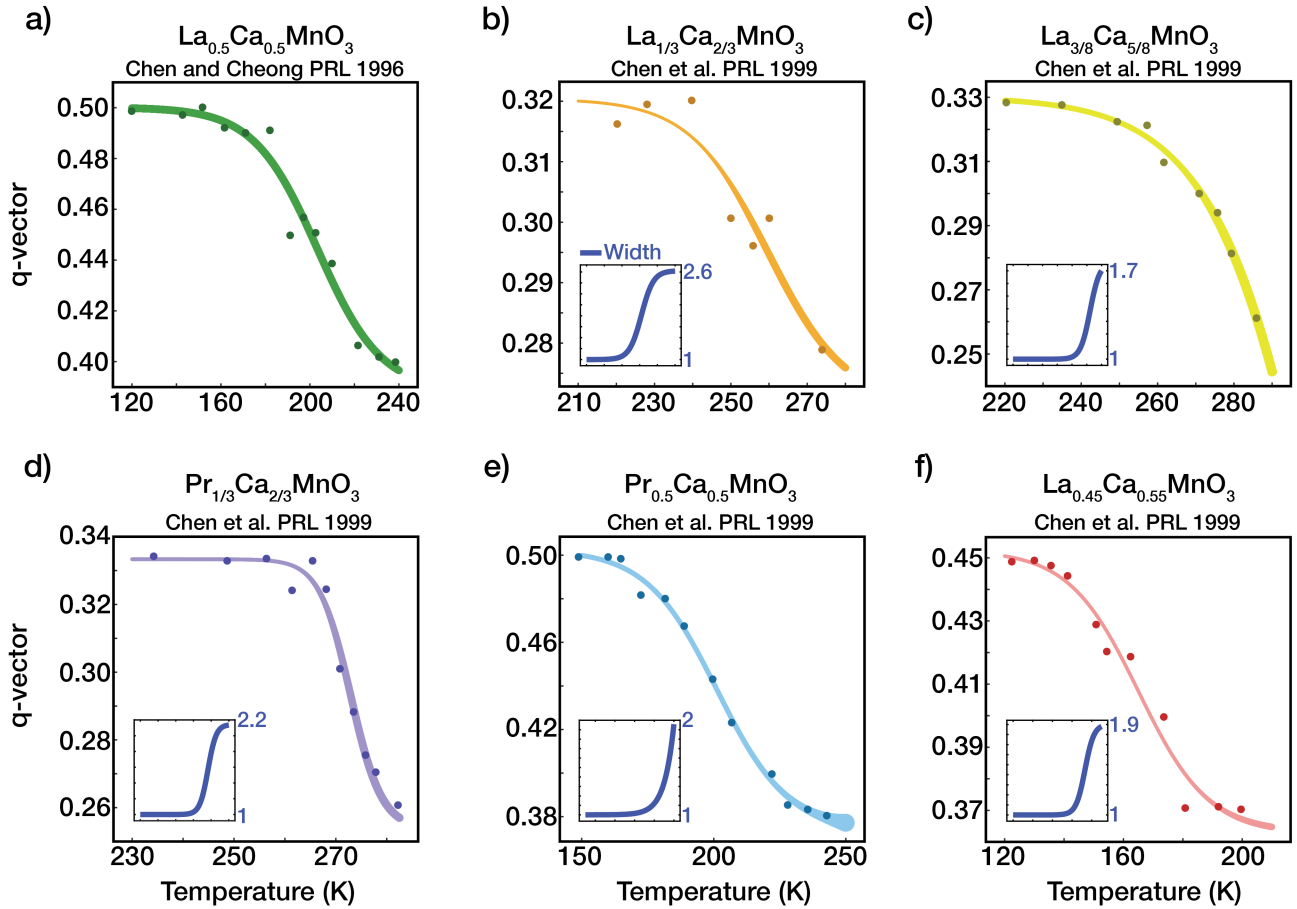
Supplementary Figure 1 | Melting of 2D Crystal with Volume Expansion and Charge Removal. a–c) Classical melting of 2D crystal with volume expansion. Topological defects occupy increased volume, driving an increased average lattice spacing. CDW amplitude collapses near topological sites. In the discrete charge crystal representation, amplitude collapse is modeled as the removal of charge centers. At constant temperature and pressure, reducing particle count accommodates a volume reduction (c–e). The volume of melted state (e) is equal to that of the ordered state (a), and there is a 23% site reduction. The reduction in particle count at a fixed volume increases the average lattice spacing.

2 Extended Meta-Analysis on CDW Melting



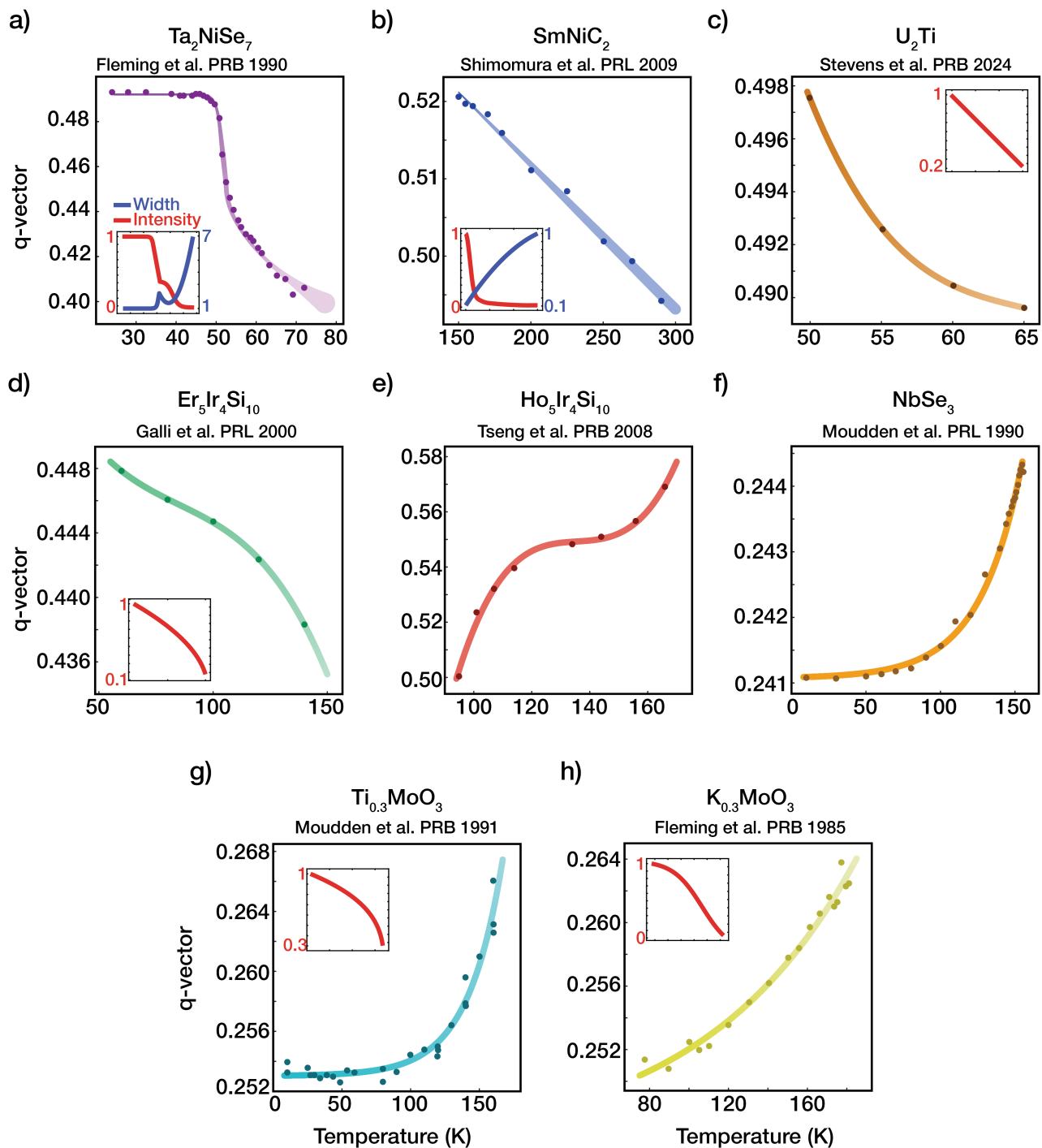
Supplementary Figure 2 | Melting of 2D CDWs. Wavevector contraction is present in layered tellurides¹ **a)**, 2D metals^{2,3} **b,c)**, and other anisotropic, layered materials⁴⁻⁶ **d-f)**. The 2D CDW in $NbSe_3$ and 3D (quasi-2D) CDW in CuV_2S_4 also report wavevector contraction^{7,8}. Onset of the CDW is sometimes reported (**b**, **c**), hence the initial increase in integrated intensity. **b)** Surprisingly, the width of the superlattice peak actually decreases. **f)** Falkowski et al. reports differences in measured wavevector for the positive +q (left, blue) and negative -q (right, gold). Fitted lines are guides to the eye, where line width and color intensity is proportional to CDW peak width and integrated intensity respectively (if reported).

3 Extended Meta-Analysis on CDW Melting in Manganites



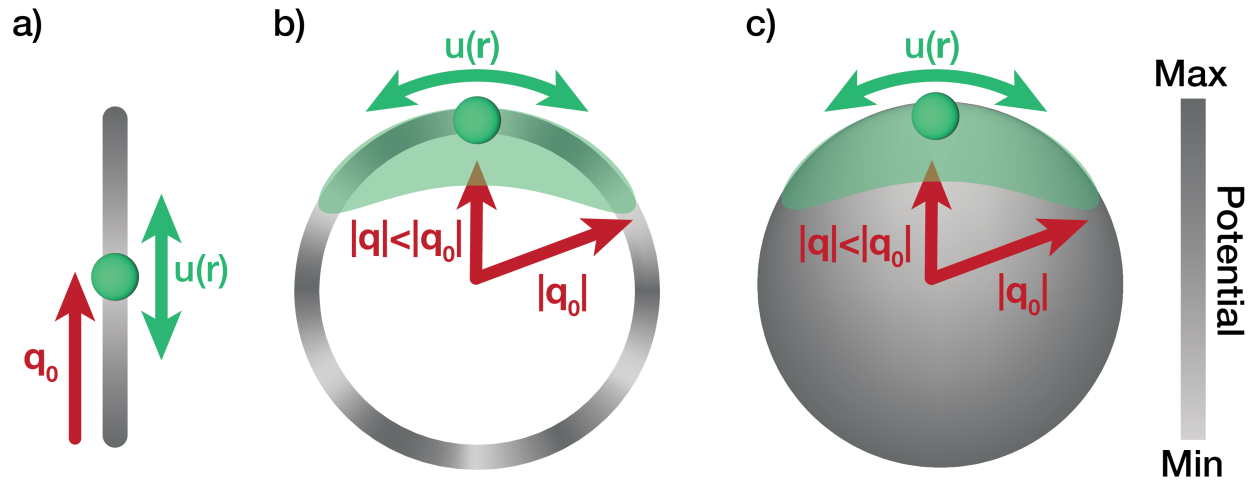
Supplementary Figure 3 | Melting of 2D CDWs in Manganites. a–f) CDW melting in manganites from^{9–11}. All reported manganite systems melt with a wavevector contraction and, when provided, azimuthal blurring of the peaks. Fitted lines are guides to the eye, where line width and color intensity is proportional to CDW peak width and integrated intensity respectively (if reported).

4 Extended Meta-Analysis on 1D CDW Melting



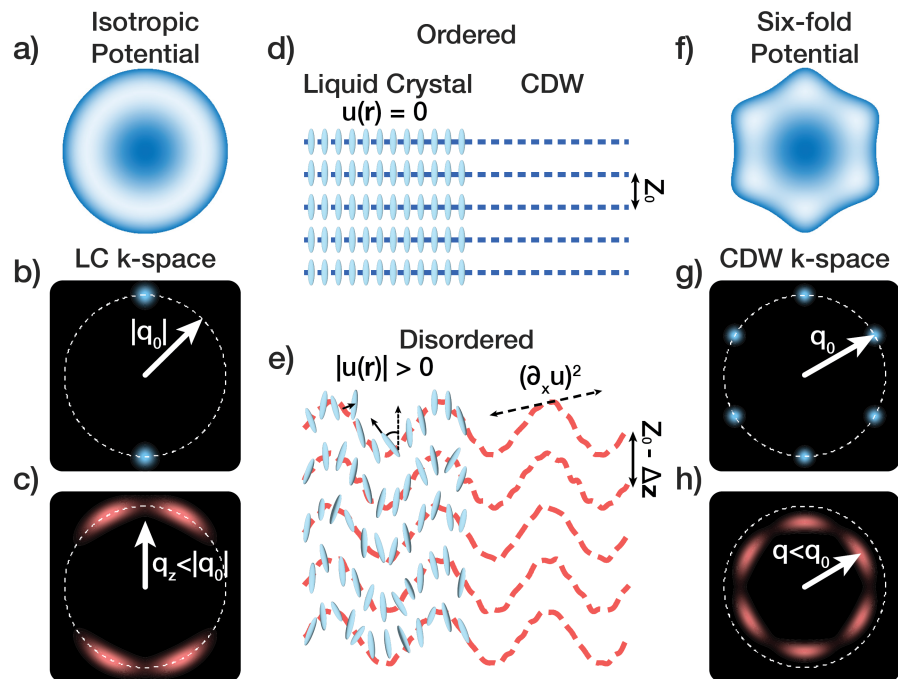
Supplementary Figure 4 | Melting of 1D CDWs. **a–c)** Wavevector contraction is observed in 1D CDW systems Ta_2NiSe_7 , SmNiC_2 , and U_2Ti ^{12–14}. The 1D CDW wavevector in ternary rare-earth metal silicides $\text{R}_5\text{Ir}_4\text{Si}_{10}$ contract with $\text{R}=\text{Er}$ ¹⁵ (**d**) and expand with $\text{R}=\text{Ho}$ ¹⁶ (**e**). Wavevector expansion is reported in the 1D CDW in NbSe_3 ¹⁷ (**f**) and blue bronzes^{18,19} **g–h**). Regardless of wavevector evolution direction, the peak width increases and the integrated intensity decreases. Fitted lines are guides to the eye, where line width and color intensity is proportional to CDW peak width and integrated intensity respectively (if reported).

5 Wavevector Contraction in Reduced Directions



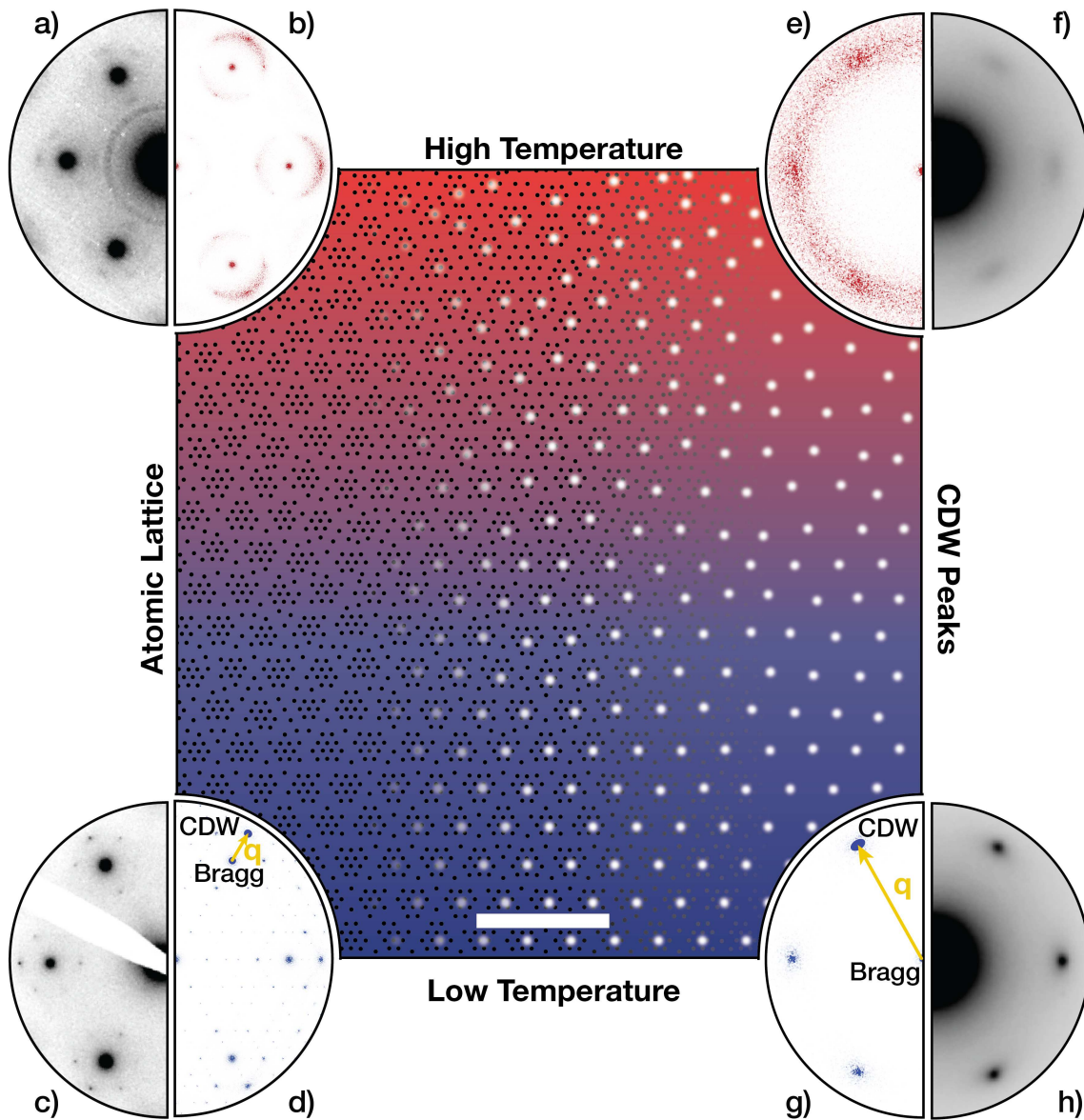
Supplementary Figure 5 | Fluctuation Effects on Wavevector in Reduced Dimensions. Reciprocal space potential landscape and wavevector behavior in (a) 1-, (b) 2-, and (c) 3- dimensions. The principal wavevector \mathbf{q}_0 sits at the minimum in the free energy. In 1D, fluctuations of the phase, $u(r)$, induce no preference for the evolution of the wavevector. Higher dimensionalities introduce convexity in the potential landscape. Fluctuations of the phase, $u(r)$ in 2D (3D) about the minimum create oscillations along a ring (sphere) of radius q_0 . Discrete rotational symmetry prevents \mathbf{q} from rotating. Rather, the wavevector smears azimuthally and contracts.

6 Liquid Crystal Melting and Continuous Rotational Symmetry



Supplementary Figure 6 | Melting of density wave in continuous and discrete rotational potentials. Potential landscape with continuous (a) and discrete (f) rotational symmetry. d, e Melting of liquid crystals (left) and CDWs (right) couple disorder in wavefront to wavelength. Ordered (b) and disordered (c) liquid crystal in k-space. The liquid crystal is free to rotate along the energy minima, and the peak in k-space splits. g, h There is a high energy cost for the CDW to rotate so the peak moves in and smears instead.

7 CDW Melting Observed in the Atomic Lattice



Supplementary Figure 7 | Melting of CDW in an Atomic Lattice. Tantalum nuclei (black spots, left) positions modulated by a progressively melted CDW (CDW peaks as white spots, right). Scale bar is 5nm. The charge lattice, too, becomes progressively disordered. The atomic lattice remains ordered but disorder manifests in the associated periodic lattice distortions. Here, the periodic lattice distortion effect is exaggerated for visual clarity. Comparison of 2D 1T-TaS₂ diffraction pattern (a, c) with simulated atomic lattice (b, d) at low and high temperatures. The \mathbf{q} -vector points from the Bragg peak to the CDW superlattice peaks. The superlattice peaks are anisotropically distributed around each Bragg peak. Averaging the six first order Bragg peaks and surrounding superlattice peaks removes the anisotropy and serves as a direct probe of the CDW (f, h). Simulated diffraction of the CDW peaks matches experimental CDW melting.

8 Free Energy of a Unidirectional CDW with 6-Fold Rotational Symmetry

For a two-dimensional system with discrete 6-fold rotational symmetry system which orders along one dimension at $|\mathbf{q}| = q_0$, the free energy can be given by²⁰:

$$H = \frac{1}{2}K \int d^2r \left\{ -2q_0^2 [\nabla m(\mathbf{r})]^2 + [\nabla^2 m(\mathbf{r})]^2 \right\} + W \int d^2r \left\{ [(\partial_x^3 - 3\partial_x \partial_z^2) m(\mathbf{r})]^2 \right\} \quad (S1)$$

where $m(\mathbf{r}) = \text{Re}\{\psi(\mathbf{r})\}$ is the real part of the system's order parameter $\psi(\mathbf{r}) = A(\mathbf{r})\exp[iq(z + u(\mathbf{r}))]$. $qu(\mathbf{r})$ are fluctuations of the phase. Fluctuations in the amplitude will be neglected ($A(\mathbf{r}) = A$) as we are focusing on fluctuating displacements of the wavefront ($u(\mathbf{r})$) which are prevalent in 2D CDW melting. Notably, we modify the free energy by including a sixth-order term in m :

$$(\partial_x^3 - 3\partial_x \partial_z^2) m(\mathbf{r}). \quad (S2)$$

This term encodes the six-fold rotational symmetry of our system, creating an energy landscape in Fourier space as $q^6 \cos(6\theta)$ (Fig. 4f).

Expanding the terms in the first integral individually we find that

$$-2q_0^2 [\nabla m(\mathbf{r})]^2 = -A^2 \left\{ \underline{q_0^2 q^2 [(\partial_x u)^2 + (\partial_z u)^2]} + \underline{q_0^2 q^2} + \underline{2q_0^2 q^2 \partial_z u} \right\}, \quad (S3)$$

and

$$\begin{aligned} [\nabla^2 m(\mathbf{r})]^2 = A^2 \left\{ \frac{1}{2}q^4 + \frac{1}{2}q^4 (\partial_x u)^4 + \underline{q^4 (\partial_z u)^2} + \underline{q^4 (\partial_x u)^2} + \underline{2q^4 (\partial_z u)} + \underline{2q^4 (\partial_z u)^2} + \underline{2q^4 \partial_z u (\partial_x u)^2} \right. \\ \left. + \underline{\frac{1}{2}q^2 (\partial_x^2 u)^2} + \underline{\frac{1}{2}q^2 (\partial_z^2 u)^2} + \underline{\frac{1}{2}q^4 (\partial_z u)^4} + \underline{2q^4 (\partial_z u)^3} + \underline{q^4 (\partial_x u)^2 (\partial_z u)^2} + \underline{q^2 (\partial_x^2 u) (\partial_z^2 u)} \right\}. \quad (S4) \end{aligned}$$

Note here that we have averaged over one period such that $\cos^2(qz + qu(\mathbf{r}))$ and $\sin^2(qz + qu(\mathbf{r}))$ average to $\frac{1}{2}$ and $\cos(qz + qu(\mathbf{r})) \sin(qz + qu(\mathbf{r}))$ average to zero. Further, all underlined terms are those which are kept in the expansion as we neglect higher-order terms such as $(\partial_z u)^4$, $(\partial_z u)^3$, $(\partial_z^2 u)^2$ and $(\partial_x u)^2 (\partial_x u)^2$ since these do not affect the long-range behavior of our system^{20,21}. Grouping these remaining terms together we have:

$$\begin{aligned} H = \frac{1}{2}KA^2 \int d^2r \left\{ q^4 \left[\frac{1}{2} - \frac{q_0^2}{q^2} \right] + 2q^4 [(\partial_z u) - q^{-2}q_0^2 (\partial_z u)] + q^4 [(\partial_x u)^2 + (\partial_z u)^2 - q^{-2}q_0^2 ((\partial_x u)^2 + (\partial_z u)^2)] \right. \\ \left. + \frac{q^2}{2} [(\partial_x^2 u)^2] + 2q^4 [(\partial_z u)^2] + 2q^4 [\partial_z u (\partial_x u)^2] + \frac{q^4}{2} [(\partial_x u)^4] \right\}. \quad (S5) \end{aligned}$$

Assuming the wavevector q will shift negligibly, we can set $q = q_0$:

$$H = \frac{1}{2}KA^2 q_0^4 \int d^2r \left\{ C_0 (\partial_x u)^2 + \frac{1}{2q_0^2} (\partial_x^2 u)^2 + 2(\partial_z u)^2 + 2\partial_z u (\partial_x u)^2 + \frac{1}{2} (\partial_x u)^4 \right\}. \quad (S6)$$

Note we have dropped the constant term $-\frac{1}{2}q_0^4$ in H since it does not affect any conclusions on the behavior of our system. We will now determine the factor C_0 . To start, we expand $(\partial_x^3 - 3\partial_x \partial_z^2) m(\mathbf{r})$, neglecting any terms of order $O(u^3)$ and higher. This leaves us with

$$\begin{aligned} (\partial_x^3 - 3\partial_x \partial_z^2) m(\mathbf{r}) = A^2 \left\{ 18q_0^4 (\partial_x \partial_z u)^2 + \underline{\frac{9}{2}q_0^6 (\partial_x u)^2} + \frac{1}{2}q_0^2 (\partial_x^3 u)^2 + \frac{9}{2}q_0^2 (\partial_x \partial_z^2 u)^2 - 9q_0^4 (\partial_x u) (\partial_x \partial_z^2 u) \right. \\ \left. + 3q_0^4 (\partial_x u) (\partial_x^3 u) - 3(\partial_x \partial_z^2 u) (\partial_x^3 u) \right\} + O(u^3). \quad (S7) \end{aligned}$$

Further, we will only keep the lowest order term, $(\partial_x u)^2$ (underlined), since this is the term of interest and all other terms are of higher order:

$$(\partial_x^3 - 3\partial_x \partial_z^2) m(\mathbf{r}) = A^2 \frac{9}{2} q_0^6 (\partial_x u)^2 + \text{higher order terms} \quad (S8)$$

This term represents a correction to the $(\partial_x u)^2$ term induced by the six-fold symmetry of our system. With this correction we have for C_0 :

$$C_0 = \frac{1}{q_0^2} \left(\frac{K}{2} q_0^2 - \frac{K}{2} q_0^2 + W \frac{9}{2} q_0^4 \right) = W \frac{9}{2} q_0^2. \quad (S9)$$

We note that, aside from $(\partial_z u)$, other coefficients of the terms in the expansion will also have similar corrections. We neglect these corrections as they do not cause the system's behavior to deviate from that of the system with continuous rotational symmetry. With these corrections we return to the final expression from the main text:

$$H = \frac{1}{2} K A^2 q_0^4 \int d^2 r \left\{ C_0 (\partial_x u)^2 + \frac{1}{2 q_0^2} (\partial_x^2 u)^2 + 2 (\partial_z u)^2 + 2 \partial_z u (\partial_x u)^2 + \frac{1}{2} [(\partial_x u)^2]^2 + \text{higher order terms} \right\} \quad (\text{S10})$$

References

1. Shin, K. Y. *et al.* Observation of two separate charge density wave transitions in Gd_2Te_5 via transmission electron microscopy and high-resolution X-ray diffraction. *J. Alloys Compd.* **489**, 332–335 (2010).
2. Fleming, R. M., ter Haar, L. W. & DiSalvo, F. J. X-ray scattering study of charge-density waves in $\text{K}_3\text{Cu}_8\text{S}_6$. *Phys. Rev. B* **35**, 5388–5391 (1987).
3. Sato, H., Kojima, N. & Kagoshima, S. Structural Phase Transitions of the Quasi Two-Dimensional Metal $(\text{K}_{1-x}\text{Rb}_x)\text{Cu}_8\text{S}_6$: X-Ray Scattering Studies. *J. Phys. Soc. Japan* **62**, 2051–2061 (1993).
4. Souliou, S. M. *et al.* Soft-Phonon and Charge-Density-Wave Formation in Nematic BaNi_2As_2 . *Phys. Rev. Lett.* **129**, 247602 (2022).
5. Lee, J. *et al.* Charge density wave with anomalous temperature dependence in UPt_2Si_2 . *Phys. Rev. B* **102**, 041112 (2020).
6. Falkowski, M., Doležal, P., Andreev, A. V., Duverger-Nédellec, E. & Havela, L. Structural, thermodynamic, thermal, and electron transport properties of single-crystalline LaPt_2Si_2 . *Phys. Rev. B* **100**, 064103 (2019).
7. Brun, C., Wang, Z.-Z., Monceau, P. & Brazovskii, S. Surface Charge Density Wave Phase Transition in NbSe_3 . *Phys. Rev. Lett.* **104**, 256403 (2010).
8. Fleming, R. M., DiSalvo, F. J., Cava, R. J. & Waszczak, J. V. Observation of charge-density waves in the cubic spinel structure CuV_2S_4 . *Phys. Rev. B* **24**, 2850–2853 (1981).
9. Chen, C. H. & Cheong, S.-W. Commensurate to Incommensurate Charge Ordering and Its Real-Space Images in $\text{La}_{0.5}\text{Ca}_{0.5}\text{MnO}_3$. *Phys. Rev. Lett.* **76**, 4042–4045 (1996).
10. Chen, C. H., Mori, S. & Cheong, S.-W. Anomalous Melting Transition of the Charge-Ordered State in Manganites. *Phys. Rev. Lett.* **83**, 4792–4795 (1999).
11. Milward, G. C., Calderón, M. J. & Littlewood, P. B. Electronically soft phases in manganites. *Nature* **433**, 607–610 (2005).
12. Fleming, R. M., Sunshine, S. A., Chen, C. H., Schneemeyer, L. F. & Waszczak, J. V. Defect-inhibited incommensurate distortion in Ta_2NiSe_7 . *Phys. Rev. B* **42**, 4954–4959 (1990).
13. Shimomura, S. *et al.* Charge-Density-Wave Destruction and Ferromagnetic Order in SmNiC_2 . *Phys. Rev. Lett.* **102**, 076404 (2009).
14. Stevens, C. R., Hermann, A., Huxley, A. & Wermeille, D. Incommensurate charge density wave order in U_2Ti . *Phys. Rev. B* **109**, 125116 (2024).
15. Galli, F. *et al.* Charge-Density-Wave Transitions in the Local-Moment Magnet $\text{Er}_5\text{Ir}_4\text{Si}_{10}$. *Phys. Rev. Lett.* **85**, 158–161 (2000).
16. Tseng, C. M., Chen, C. H. & Yang, H. D. Direct observation of charge-density waves in $\text{Ho}_5\text{Ir}_4\text{Si}_{10}$. *Phys. Rev. B* **77**, 155131 (2008).
17. Moudén, A. H., Axe, J. D., Monceau, P. & Levy, F. q_1 charge-density wave in NbSe_3 . *Phys. Rev. Lett.* **65**, 223–226 (1990).
18. Moudén, A. H., Elmiger, M., Shapiro, S. M., Collins, B. T. & Greenblatt, M. Neutron-scattering investigation of the charge-density wave in $\text{Tl}_{0.3}\text{MoO}_3$. *Phys. Rev. B* **44**, 3324–3327 (1991).
19. Fleming, R. M., Schneemeyer, L. F. & Moncton, D. E. Commensurate-incommensurate transition in the charge-density-wave state of $\text{K}_{0.30}\text{MoO}_3$. *Phys. Rev. B* **31**, 899–903 (1985).
20. Grinstein, G. & Pelcovits, R. A. Anharmonic Effects in Bulk Smectic Liquid Crystals and Other “One-Dimensional Solids”. *Phys. Rev. Lett.* **47**, 856–859 (1981).
21. Grinstein, G. & Pelcovits, R. A. Nonlinear elastic theory of smectic liquid crystals. *Phys. Rev. A* **26**, 915–925 (1982).